NANO LETTERS

Letter

pubs.acs.org/NanoLett

Conflicting Roles of Nickel in Controlling Cathode Performance in Lithium Ion Batteries

Meng Gu,[†] Ilias Belharouak,[‡] Arda Genc,[§] Zhiguo Wang,[⊥] Dapeng Wang,[‡,∥] Khalil Amine,[‡] Fei Gao,[⊥] Guangwen Zhou,[∥] Suntharampillai Thevuthasan,[†] Donald R. Baer,[†] Ji-Guang Zhang,[#] Nigel D. Browning,[⊥] Jun Liu,[⊥] and Chongmin Wang*,[†]

[†]Environmental Molecular Science Laboratory, [⊥]Fundamental and Computational Science Directorate, and [#]Energy and Environmental Directorate, Pacific Northwest National Laboratory, 902 Battelle Boulevard, Richland, Washington 99352, United States

[‡]Chemical Sciences and Engineering Division, Argonne National Laboratory, 9700 South Cass Avenue, Argonne, Illinois 60439, United States

[§]FEI Company, 5350 NE Dawson Creek Drive, Hillsboro, Oregon 97124, United States

[∥]Department of Mechanical Engineering, Binghamton University, State University of New York, Binghamton, New York 13902, United States

Supporting Information

ABSTRACT: A variety of approaches are being made to enhance the performance of lithium ion batteries. Incorporating multivalence transition-metal ions into metal oxide cathodes has been identified as an essential approach to achieve the necessary high voltage and high capacity. However, the fundamental mechanism that limits their power rate and cycling stability remains unclear. The power rate strongly depends on the lithium ion drift speed in the cathode. Crystallographically, these transition-metal-based cathodes frequently have a layered structure. In the classic wisdom, it is accepted that lithium ion travels swiftly within the layers moving out/in of the cathode during the charge/discharge. Here, we report the unexpected discovery of a thermodynamically driven, yet kinetically controlled, surface modification in the widely explored lithium nickel manganese oxide cathode material, which may inhibit the battery charge/discharge rate. We found that during cathode synthesis and processing before electrochemical cycling in the cell nickel can preferentially move along the fast diffusion channels and selectively segregate at the surface facets terminated with a mix of anions and cations. This segregation essentially can lead to a higher lithium diffusion barrier near the surface region of the particle. Therefore, it appears that the transition-metal dopant may help to provide high capacity and/or high voltage but can be located in a "wrong" location that may slow down lithium diffusion, limiting battery performance. In this circumstance, limitations in the properties of lithium ion batteries using these cathode materials can be determined more by the materials synthesis issues than by the operation within the battery itself.

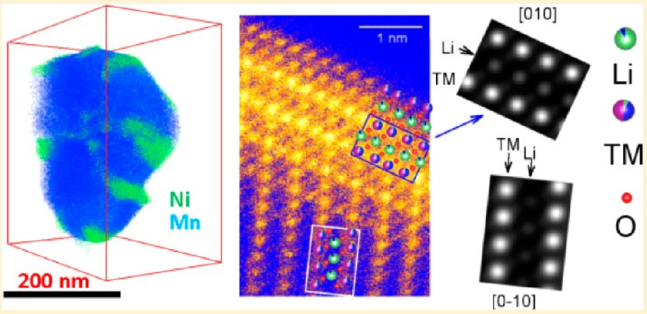

KEYWORDS: *Lithium ion battery, $Li_{1.2}Ni_{0.2}Mn_{0.6}O_2$, nickel segregation, STEM, DFT calculation, lithium diffusion barrier*

Lithium ion batteries have been widely used in consumer electronics and have entered the electrical vehicle market due to their high energy density.[1−3] However, their power rate and cycle life still need to be improved for long-term applications. The power rate of the lithium (Li) ion batteries strongly depends on the rate of Li^+ diffusion within the cathode structure.[1,4−6] Significant efforts have been made to improve the power rate of Li ion batteries by doping cathodes to increase electronic conductivity,[6] reducing the Li ion diffusion distances by using nanoscale particles,[6,7] surface coating,[1] and enhancing surface facets with Li^+ fast-diffusion channels.[8] Lithium transition-metal oxides have been widely used as the cathode for Li ion batteries. They can be tailored to gain either high voltage or high capacity by adjusting the relative ratio of different transition-metal ions and preparation conditions.[9−20] For example, a layered composite based on lithium nickel manganese oxide $Li_{1.2}Ni_{0.2}Mn_{0.6}O_2$ (LNMO) has demonstrated a rechargeable capacity of >250 mAh/g, which is much larger than that of the conventional $LiCoO_2$ cathode (<140 mAh/g).[10,14,16,21,22] This category of material is featured by a layered composite structure in which the channels within the structure can act as a low-barrier path for Li ions to move during the

Received: June 15, 2012
Revised: August 22, 2012
Published: September 17, 2012

 © 2012 American Chemical Society

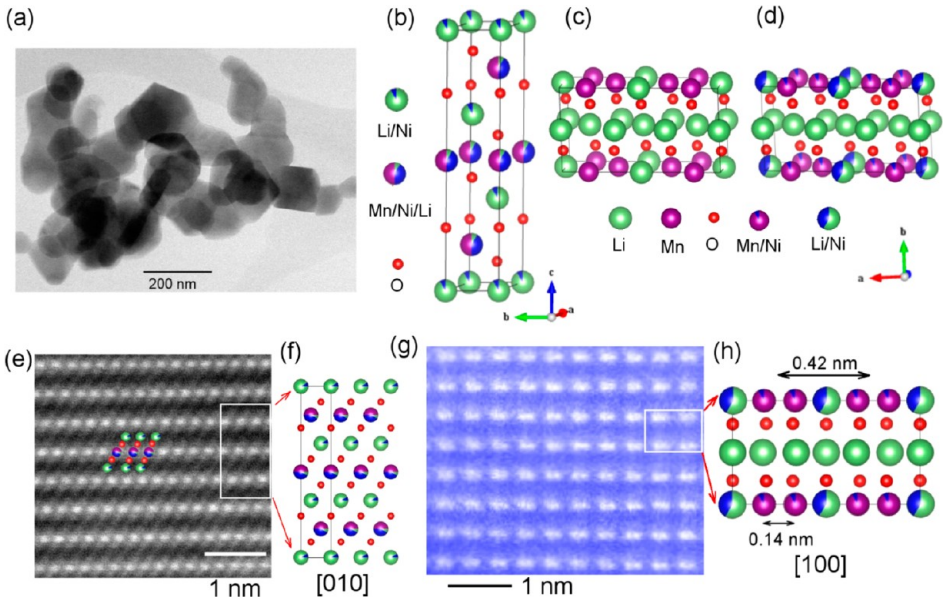

Figure 1. (a) Overview bright-field scanning transmission electron microscopy (STEM) image of the as-obtained LNMO nanoparticles. (b) Crystal model for the $LiMO_2$ $R\bar{3}m$ parent phase based on a $Li(Mn_{0.5}Ni_{0.5})O_2$ structure with lattice parameters: $a = b = 2.887$ Å, $c = 14.29$ Å, $\alpha = \beta = 90°$, and $\gamma = 120°$.[24] (c) Crystal model for Li_2MO_3 $C2/m$ parent phase based on Li_2MnO_3 with lattice parameters: $a = 4.926$ Å, $b = 8.527$ Å, $c = 5.028$ Å, $\alpha = \gamma = 90°$, and $\beta = 109.22°$.[24] (d) Partially cation-ordered Li_2MO_3 $C2/m$ phase based on Ni-containing Li_2MnO_3.[16] (e) Z-contrast image of one sample region corresponding to (f) [010] zone projection of the $LiMO_2$ $R\bar{3}m$ model. (g) Crystal region corresponding to (h) [100] zone projection of the Ni-doped Li_2MnO_3 $C2/m$ phase.

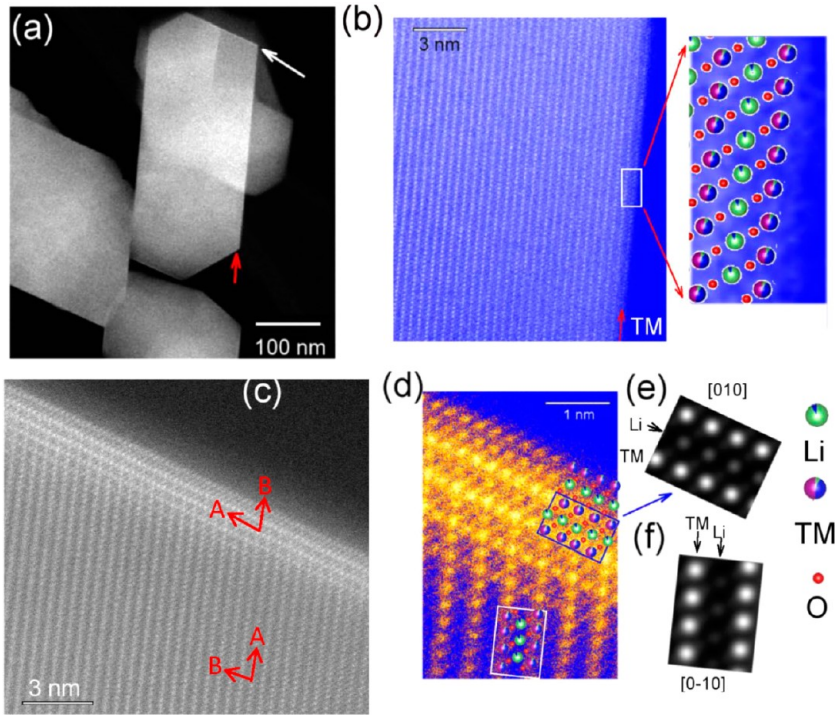

Figure 2. (a) Overview Z-contrast image of LNMO nanoparticles. (b) Atomic resolution Z-contrast image of the surface region labeled by the red arrow in (a). (c) Atomic resolution Z-contrast image of the surface region labeled by the white arrow in (a). (d) Higher magnification image of the surface layer shown in (c). (e) Simulated [010] zone projection Z-contrast image based on $LiNi_{0.5}Mn_{0.5}O_2$ crystal model with 20% Ni/Li disorder corresponding to the region labeled with blue rectangle in (d). (f) Simulated [0−10] zone projection Z-contrast image based on $LiNi_{0.5}Mn_{0.5}O_2$ crystal model with 10% Ni/Li disorder corresponding to the region labeled with a white rectangle in (d). TM is transition metal. Letters A and B in (c) marks two typical Li diffusion paths. The path A is a fast diffusion channel within the layer.

charge/discharge processes.[5] Here we report our surprising discovery of a selective surface lattice plane segregation of nickel (Ni) ions for the case of LNMO as a representative case for the transition-metal oxide-based cathode and the possible implications of such a surface segregation on the Li ion transport behavior in this category of cathode material. What we have observed is a phenomenon that is far beyond general expectation and will broadly impact the research effort for

dx.doi.org/10.1021/nl302249v | Nano Lett. 2012, 12, 5186−5191

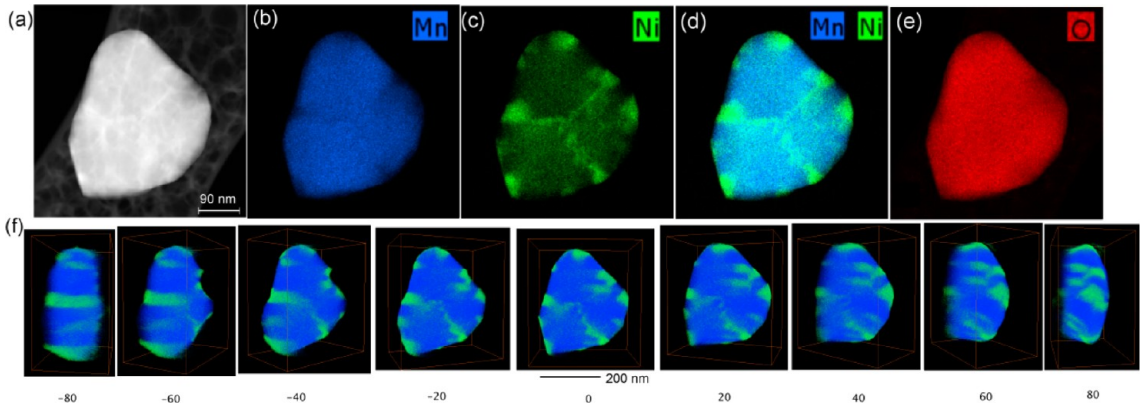

Figure 3. (a) Z-contrast image of a nanoparticle with internal grain boundaries and XEDS maps: (b) Mn, (c) Ni, (d) overlaid Ni and Mn, and (e) O maps (f) 3D XEDS tomography: reconstructed Mn and Ni elemental distribution maps projected at different angles showing that the Ni segregated to certain surfaces and grain boundaries.

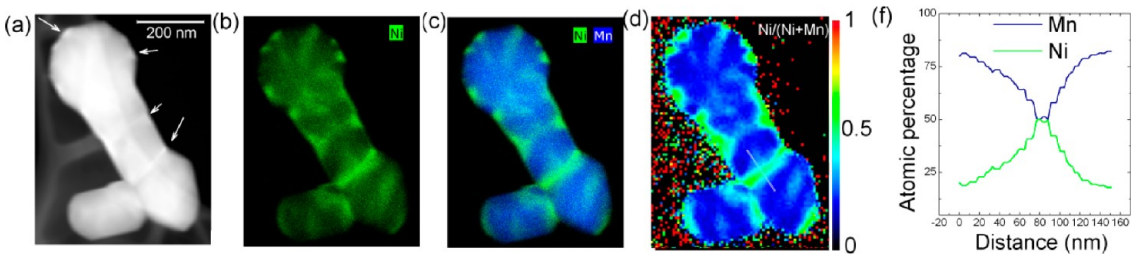

Figure 4. Z-contrast image and XEDS maps of multiple nanoparticle aggregate; (a) Z-contrast image, (b) Ni, (c) overlayed Ni and Mn, and (d) Ni/(Mn + Ni) atomic percentage quantification maps. (f) Atomic percentage of Mn and Ni along the white line in (f). The scale bar in (a) applies to all the images.

enhancing the rate performance of Li ion batteries and stability of cathode in the electrolyte.

As shown in the overview image in Figure 1a, the as-synthesized LNMO nanoparticles assume a plate-like shape and a significant number of the particles exhibit good surface facets. As reported, LNMO structure comprises two components as shown in Figure 1b−d: monoclinic Li_2MO_3 $C2/m$ and trigonal $LiMO_2$ $R\bar{3}m$ (α-$NaFeO_2$ structure) (M = transition metal).[11,14,23−25] Both phases belong to a layered structure composed of repeating transition-metal layers, oxygen layers and Li layers as shown in Figure 1b−d. In the $R\bar{3}m$ structure (Figure 1b), Ni and Li are located at both the 3a and 3b sites, whereas Mn is located only at the 3a site (using Wyckoff notation).[24,26] On the other hand, in the cation ordered Li_2MO_3 $C2/m$ structure (Figure 1c), the larger Ni^{2+} cations preferably replace the Li^+ cations in the transition-metal layer (2b sites) and a small portion of Mn cations as shown in Figure 1d. We found that most of the region of the particle adopts the α-$NaFeO_2$ $R\bar{3}m$ structure in which the transition-metal layer has the highest contrast in the high angle annular dark field (HAADF) Z-contrast image in Figure 1e,f, while the oxygen layers can be clearly visualized on both sides of the transition-metal column. Due to the much smaller atomic number of Li, it cannot be clearly seen in the Z-contrast image Figure 1e,f. Partially ordered Li_2MO_3 $C2/m$ phase is also observed in part of the particle. The Z-contrast image in Figure 1g unambiguously identifies the partially cation-ordered region corresponding to the [100] zone projection of the Ni-containing Li_2MnO_3 $C2/m$ structure model in Figure 1h. This structure is well-characterized by two bright Mn columns separated by 0.14 nm and the center of two neighboring Mn/Ni dumbbell columns spaced by 0.42 nm.[16,23,27]

In the Z-contrast image, we noticed that for a single particle, some faceting planes are brighter than the others as typically shown in Figure 2a, in which two facets adjacent to each other were labeled with white and red arrows. Figure 2b is the atomic resolution image of the red arrowed facet, revealing that this facet corresponds to the (001) plane and is terminated at transition-metal ions. On the other hand, the white arrowed facet corresponds to the (104) plane of the particle and is characterized by a surface layer with a higher contrast than the interior of the particle as shown in Figure 2c. The higher Z-contrast of this surface layer indicates a high concentration of heavy elements, Ni (Z_{Ni} = 28 compared to Z_{Mn} = 25 and Z_{Li} = 3) at the surface. An atomic resolution Z-contrast image combined with the multislice image simulations as illustrated in Figure 2d−f reveals that this surface layer corresponds to the [010] zone axis projection of $R\bar{3}m$ crystal structure. This surface capping layer is oriented such that the otherwise mix of cations and anions terminated (104) facet of the particle is also terminated with a transition-metal layer as is similarly the case of (001) plane. This observation clearly demonstrates that if the termination surface ends up with a transition-metal layer (such as (001) surface), there is no surface modification layer as shown by Figure 2b. On the other hand, if the particle surface is terminated with a mix of cations and anions, a surface capping layer is formed by preferential segregation of Ni ions, which eventually leads to the termination of the particle facet as transition-metal ions.

The selective surface modification associated with Ni segregation is consistently supported by the quantitative

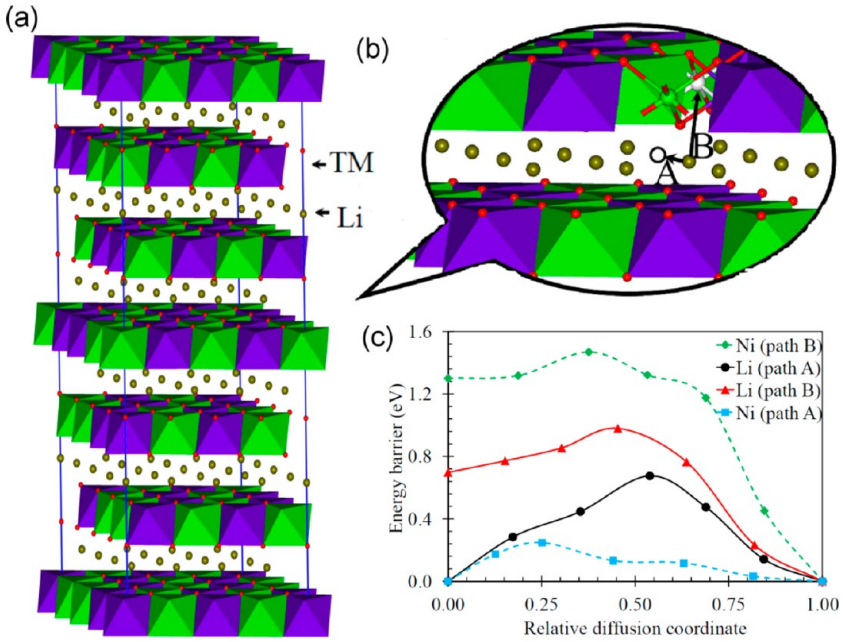

Figure 5. (a) Crystal model of the $LiNi_{0.5}Mn_{0.5}O_2$ structure defined for the calculation. (b) Different diffusion paths for Li and Ni diffusion. Note that at the end of paths A and B are a Li and a transition-metal vacancy site. (c) Energy barrier along the diffusion paths A and B.

composition analysis using large-area X-ray energy dispersive spectroscopy (XEDS) mapping and tomography (Figures 3 and 4). The Z-contrast images at 0° tilt in Figure 3a show that the grain boundaries and some surface regions exhibit an enhanced Z-contrast, implying a higher concentration of Ni. Through the integration of Mn, Ni, and O K_α peaks, element specific quantitative maps were obtained and are shown in Figure 3b−e. Most surprisingly, the Ni distribution is extremely uneven; while rich in grain boundaries and certain surface regions, it is deficient in the interior of the particles. The average Ni:Mn ratio is 1:3 as quantified using peak integrated XEDS spectra of the whole particle, which corresponds well to the Ni:Mn ratio in the nomnal composition $Li_{1.2}Ni_{0.2}Mn_{0.6}O_2$. A series of XEDS maps were also acquired at 5° tilt increments from −70° to +70° and reconstructed to provide a 3D visualization of the Ni and Mn distribution in the LNMO nanoparticle. The 3D morphological structure and the spatial distribution of the segregated Ni of a single LNMO particle are illustrated by the overlaid Mn and Ni maps projected at different tilt angles of the reconstructed LNMO nanoparticle (Figure 3f). The animated 3D visualization of the chemical mapping of the nanoparticle is in the Supporting Information movie. It reveals that the Ni ions are selectively segregated at certain surface locations and grain boundaries. This is further supported by the XEDS chemical analysis in a region with several nanoparticle aggregates as illustrated in Figure 4. The XEDS quantification reveals that the Ni/Mn ratio ranges from ∼1:4 inside the particle to ∼1:1 in certain surfaces or grain boundaries in Figure 4f. It should be pointed out that Xu et al.[28] have studied the surface structure of the LNMO particle following the charge/discharge cycles. They noticed that a surface layer was formed on the particle due to substitution of Li ions by transition metal cations and formation of spinal structure. As we are focusing on the freshly prepared sample, we do not see any formation of spinel at the surface region of the particles.

What we have observed in this work contrasts markedly with the general observation of other multicomponent nanoparticles for which the segregating species tend to uniformly cover the whole nanoparticle surface, leading to a core−shell structure.[29,30] This interesting selective surface modification phenomenon is related to the surface energies of different terminations and the diffusion kinetics of Ni cations within the layered structure. As calculated by Wei et al.,[8] for a similar composition crystal, $Li[Li_{0.17}Ni_{0.25}Mn_{0.58}]O_2$, the (001), a surface ending with a transition-metal layer has a lower surface energy and, therefore, is thermodynamically more stable. On the other hand, the surfaces ending with alternating transition-metal, oxygen, and Li layers are not thermodynamically stable. We used DFT to calculate the diffusion energy barriers of Li^+ across different paths. It should be pointed out that the diffusion energy barrier shows dependence on diffusion mechanisms and overall elemental composition. For example, Li diffusion in layered intercalation compounds, such as Li_xCoO_2 and Li_xTiS_2, is a divacancy-mediated mechanism.[31−33]

Here, the calculation is based on the $LiNi_{0.5}Mn_{0.5}O_2$ $R\bar{3}m$ model as shown in Figure 5a (details of the calculations are described in the Supporting Information). Two different paths are considered for Li migration in this layered structure through cation vacancy migration, as shown in Figure 5b. Path A is parallel to the Li^+ layer involving an in-plane jump from the start site to the nearby vacancy site in the Li^+ layer. As Li^+ can also reside at the transition-metal layer, the jump from Li site to a Ni vacancy is also considered, which indicates an off-plane jump (path B). In Figure 2c, these two possible Li diffusion paths A and B are labeled with arrows in the bulk crystal and surface layers. Those two diffusion paths are also considered for Ni migration. As Li or Ni ions move from one octahedral site to another, it will pass through an intermediate tetrahedral site where it encounters the repulsion from a nearby transition-metal cation. The energy barrier for Ni or Li diffusion should be related to the different degrees of repulsion from the transition-metal cation. As shown in Figure 5c, the energy barriers for both Li and Ni diffusion along path A are much lower than path B, consistent with previous models for diffusion in this system.

The calculation in Figure 5c shows that the energy barrier for Ni to diffuse along the Li channel is ~0.25 eV; therefore, it is very easy for Ni to diffuse to the surface once Ni is in the Li^+ layer. In contrast, the diffusion energy barrier for Ni to diffuse along path B is as high as 1.47 eV, implying that Ni is not very likely to diffuse along path B. Similarly, the diffusion barrier for Li^+ along path A parallel with the Li^+ layer is around 0.67 eV compared to 0.98 eV along path B. This result corresponds well with earlier reports regarding to the Li^+ fast diffusion paths.[34] Most importantly, the diffusion barrier for Ni along the Li^+ layer is smaller than Li^+, implying that Ni diffusion along the Li^+ channels is even easier. Taken together, these results explain the experimentally observed selective Ni segregation and corresponding surface modification phenomenon described above in Figures 2 and 3.

The charge/discharge rate of a cathode material is critically controlled by the Li ion mobility in the lattice. Theoretical calculations and experimental observation have established that in the layer structured cathode, Li ion diffusion along the layer is much easier than across the layer.[5,28,31−33] The channels within the surface layer formed on the nanoparticle are approximately perpendicular to the channels inside the particle (relative rotation angle of ~109.5°). Therefore, the formation of the surface layer should lead to a diffusion barrier for Li at the particle surface region. Consequently, from all we know of the mechanism of charging/discharging, this surface layer should affect the charge/discharge rate of the battery. Of course, to quantify this link, more systematic experimental work should be performed to examine the effect of nanoscale chemical inhomogeneities and structural variations within a single particle on the overall battery performance. The present observations clearly indicate that this Ni surface modification phenomenon can occur during material synthesis. As cation diffusion is highly related to the synthesis temperature and high-temperature growth time, optimizing these material processing parameters may decrease the level the segregation related surface layer. Several approaches were employed in this study (sol−gel, hydrothermal, and coprecipitation) that incorporated a wide variation in the synthesis conditions for the LNMO system. All the LNMO synthesized for our analysis showed some degree of Ni segregation. In a typical example, we mixed $Ni_{0.25}Mn_{0.75}(OH)_2$ and Li_2CO_3, and the mixture was calcined at 900 °C for different times. Microscopically, we found that with a longer calcination time, the particles are prone to possess well-defined facets and show Ni segregations. The charge/discharge rate of batteries using these materials shows a dependence on the calcination time of the LNMO particles: the longer of the calcination time, the poorer the rate performance. It should be noted that the poor rate for the particles with a longer calcination time is also related to the large particle size. Clarification of the exact roles of surface segregation and particle size on the rate of the battery performance will be the focus of future work. Further and more broadly, this surface modification phenomenon may also be present in other composite cathode materials and may alter the Li ion diffusion channels. Therefore, the present observation of selective surface segregation will impact the general approach for tailoring cathode structures for a high capacity and a high power rate.

■ ASSOCIATED CONTENT

Supporting Information

Supporting movie, synthesis procedure of LNMO nanoparticles, experimental procedure for the STEM XEDS mapping and tomographic reconstruction, multislice STEM image simulations, and DFT calculation of Li^+ diffusion energy barrier. This material is available free of charge via the Internet at http://pubs.acs.org

■ AUTHOR INFORMATION

Corresponding Author

*E-mail: Chongmin.Wang@pnnl.gov

Notes

The authors declare no competing financial interest.

■ ACKNOWLEDGMENTS

M.G. wants to thank Dr. Chengyu Song from NCEM for technical support on the TEAM 0.5 microscope and Dr. Paul Plachinda from the FEI Company for his help on 3D XEDS data processing and visualization. This work was supported by the Laboratory Directed Research and Development (LDRD) program of Pacific Northwest National Laboratory (PNNL). The work was conducted in the William R. Wiley Environmental Molecular Sciences Laboratory (EMSL), a national scientific user facility sponsored by DOE's Office of Biological and Environmental Research and located at PNNL. PNNL is operated by Battelle for the DOE under contract DE-AC05-76RLO1830. Part of the work performed at NCEM is supported by DOE under contract no. DE-AC02-05CH11231.

■ REFERENCES

(1) Kang, B.; Ceder, G. *Nature* **2009**, *458*, 190.
(2) Chiang, Y.-M. *Science* **2010**, *330*, 1485.
(3) Tarascon, J. M.; Armand, M. *Nature* **2001**, *414*, 359.
(4) Kang, K.; Morgan, D.; Ceder, G. *Phys. Rev. B* **2009**, *79*, 014305.
(5) Nishimura, S.-I.; Kobayashi, G.; Ohoyama, K.; Kanno, R.; Yashima, M.; Yamada, A. *Nat. Mater.* **2008**, *7*, 707.
(6) Chung, S.-Y.; Bloking, J. T.; Chiang, Y.-M. *Nat. Mater.* **2002**, *1*, 123.
(7) Delacourt, C.; Poizot, P.; Levasseur, S.; Masquelier, C. *Electrochem. Solid-State Lett.* **2006**, *9*, A352.
(8) Wei, G.-Z.; Lu, X.; Ke, F.-S.; Huang, L.; Li, J.-T.; Wang, Z.-X.; Zhou, Z.-Y.; Sun, S.-G. *Adv. Mater.* **2010**, *22*, 4364.
(9) Hinuma, Y.; Meng, Y. S.; Kang, K.; Ceder, G. *Chem. Mater.* **2007**, *19*, 1790.
(10) Reed, J.; Ceder, G. *Electrochem. Solid-State Lett.* **2002**, *5*, A145.
(11) Lu, Z.; Beaulieu, L. Y.; Donaberger, R. A.; Thomas, C. L.; Dahn, J. R. *J. Electrochem. Soc.* **2002**, *149*, A778.
(12) Wang, J.; Yao, X.; Zhou, X.; Liu, Z. *J. Mater. Chem.* **2011**, *21*, 2544.
(13) Peng, Q.; Tang, Z.; Zhang, L.; Liu, X. *Mater. Res. Bull.* **2009**, *44*, 2147.
(14) Armstrong, A. R.; Holzapfel, M.; Novák, P.; Johnson, C. S.; Kang, S.-H.; Thackeray, M. M.; Bruce, P. G. *J. Am. Chem. Soc.* **2006**, *128*, 8694.
(15) Hong, J.; Seo, D.-H.; Kim, S.-W.; Gwon, H.; Oh, S.-T.; Kang, K. *J. Mater. Chem.* **2010**, *20*, 10179.
(16) Jarvis, K. A.; Deng, Z.-Q.; Allard, L. F.; Manthiram, A.; Ferreira, P. J. *Chem. Mater.* **2011**, *23*, 3614.
(17) Wang, J.; Xia, Y.; Yao, X.; Zhang, M.; Zhang, Y.; Liu, Z. *Int. J. Electrochem. Sci.* **2011**, *6*, 6670.
(18) Hong, Y.-S.; Park, Y. J.; Ryu, K. S.; Chang, S. H.; Kim, M. G. *J. Mater. Chem.* **2004**, *14*, 1424.
(19) Zhang, L.; Zhang, Z. C.; Wu, H. M.; Amine, K. *Energy Environ. Sci.* **2011**, *4*, 2858.

(20) Sun, Y. K.; Myung, S. T.; Park, B. C.; Prakash, J.; Belharouak, I.; Amine, K. *Nat. Mater.* **2009**, *8*, 320.
(21) Thackeray, M. M. *J. Am. Ceram. Soc.* **1999**, *82*, 3347.
(22) Johnson, C. S.; Kim, J. S.; Lefief, C.; Li, N.; Vaughey, J. T.; Thackeray, M. M. *Electrochem. Commun.* **2004**, *6*, 1085.
(23) Bareño, J.; Lei, C. H.; Wen, J. G.; Kang, S. H.; Petrov, I.; Abraham, D. P. *Adv. Mater.* **2010**, *22*, 1122.
(24) Meng, Y. S.; Ceder, G.; Grey, C. P.; Yoon, W. S.; Jiang, M.; Breger, J.; Shao-Horn, Y. *Chem. Mater.* **2005**, *17*, 2386.
(25) Lei, C. H.; Bareno, J.; Wen, J. G.; Petrov, I.; Kang, S. H.; Abraham, D. P. *J. Power Sources* **2008**, *178*, 422.
(26) Islam, M. S.; Davies, R. A.; Gale, J. D. *Chem. Mater.* **2003**, *15*, 4280.
(27) Strobel, P.; Lambert-Andron, B. *J. Solid State Chem.* **1988**, *75*, 90.
(28) Xu, B.; Fell, C. R.; Chi, M. F.; Meng, Y. S. *Energy Environ. Sci.* **2011**, *4*, 2223.
(29) Wang, X. Y.; Ren, X. F.; Kahen, K.; Hahn, M. A.; Rajeswaran, M.; Maccagnano-Zacher, S.; Silcox, J.; Cragg, G. E.; Efros, A. L.; Krauss, T. D. *Nature* **2009**, *459*, 686.
(30) Skumryev, V.; Stoyanov, S.; Zhang, Y.; Hadjipanayis, G.; Givord, D.; Nogués, J. *Nature* **2003**, *423*, 850.
(31) Van der Ven, A.; Ceder, G. *J. Power Sources* **2001**, *97*−*98*, 529.
(32) Van der Ven, A.; Ceder, G.; Asta, M.; Tepesch, P. D. *Phys. Rev. B* **2001**, *64*, 184307.
(33) Van der Ven, A.; Thomas, J. C.; Xu, Q.; Swoboda, B.; Morgan, D. *Phys. Rev. B* **2008**, *78*, 104306.
(34) Islam, M. S.; Driscoll, D. J.; Fisher, C. A. J.; Slater, P. R. *Chem. Mater.* **2005**, *17*, 5085.